Applications of algebraic reconstruction techniques to crosshole seismic data

John E. Peterson,* Bjorn N. P. Paulsson,‡ and Thomas V. McEvilly*

ABSTRACT

Tomographic imaging techniques were applied to two crosshole data sets to determine the velocity structures and the reliability and resolution of the algorithms on real data. The experiments were carried out at the Retsoff salt mine in New York and at the underground radioactive waste study site at the Stripa mine facility in Sweden. The traveltimes at Restoff were high quality and were obtained over raypaths of up to 500 m in length. The structure was quite complicated with velocity contrasts up to 50 percent. The Stripa site was in granitic rock with velocity contrasts of only a few percent. The dimensions of the experiment were small with maximum ray lengths of just over 10 m. The data at this site were collected with very high accuracy, source and receiver locations were measured to better than 1.0 mm, and traveltimes were read to 0.001 ms. A number of algorithms similar to the algebraic reconstruction techniques (ART) used in medical imaging have been applied to the data. Some modifications of the algorithms, such as the application of weighting schemes, damping parameters, and curved raypaths, were performed. The resulting velocity fields were compared to the known fields and with each other to determine an optimal method. The algorithms were found to be a rapid, reliable means of reconstructing the slowness field of real data. Low-velocity zones were recovered with accuracy in location and value. It was also found that great care was necessary in application of the techniques to ensure that proper damping parameters are used and the proper number of iterations taken; otherwise poor reconstructions will result.

INTRODUCTION

In the last decade tomographic reconstruction techniques have become widely used in medical imaging applications. For example, in X-ray tomography the tissue density field of the patient is deduced by X-ray attenuation over a full range of penetration angles. As a result of the work in medicine, four major classes of reconstruction algorithms arose: the summation methods, the convolution methods, the Fourier methods, and the summation expansion methods. The last category includes the algebraic reconstruction techniques (ART). These algorithms pose the integral equation in matrix form solved using relaxation techniques, taking advantage of the sparsity of the matrix. ART algorithms are generally simple and can be easily modified to different data geometries and to restricted angular coverage. All methods assume nonrefracting, straight rays through the medium and require a full range of penetration angles for completeness. Many variations developed from the basic ideas have advantages in specific problems.

In seismology, reconstruction techniques have applications ranging from ultrasonic crosshole studies of rock properties (Bois et al., 1972; Wong et al., 1983) to reflection seismology (Fawcett and Clayton, 1984) and deep earth structure (Clayton and Comer, 1984). In these applications either the slowness field or the attenuation field is determined. Complications arise because the true raypath is usually curved due to the spatial variation of the field. In most seismological problems, restrictions on source and receiver locations limit the range of penetration angles through the volume of interest, resulting in irregular sampling. Seismological applications thus are often customized for each experiment, depending upon the available sampling and the source-to-receiver geometries.

A number of ART-type algorithms have been applied to two crosshole seismic data sets to determine the utility of such techniques in the detection of slowness anomalies in rock. The algorithms are also compared for accuracy, convergence, and reliability. ART was selected because of its facility for handling different geometries with irregular sampling or limited projection angles.

DATA

We studied two appropriate data sets available from crosshole-type experiments. Both have high-quality traveltimes from dense networks in areas where the structure is fairly well known. The experiments were carried out at the Retsoff salt mine in New York and at the underground radio-

active waste study site at the Stripa mine facility in Sweden; the anticipated anomalous velocities are due to solution processes in the former case and to heating in the latter.

The Retsoff mine data set consists of some 400 P-wave traveltimes measured along intersecting raypaths between three sets of explosion sources and geophones: on a 400 m surface line, in a borehole to a depth of 260 m, and in the mine at a depth of 320 m. The resulting array of raypaths is shown in Figure 1. The area of interest is almost entirely encircled by this geometry, but the field is not regularly sampled. The paths do not lie within an exact plane, since the mine is offset approximately 25 m from the plane of the boreholes and surface arrays. This sampled region contains a collapse zone apparently due to dissolution of overlying carbonate rocks by groundwater flow into an old shaft. It was hoped that the reconstruction would define zones of major dissolution and provide guidance on possible remedial engineering steps. The traveltime readings are accurate to within 1 ms, and the number of rays is such that the field may be discretized into 25 m square cells.

The Stripa experiment investigated the behavior of a granitic rock mass heated by an electric heater simulating a radioactive waste cannister, emplaced in a large diameter borehole in the floor of an underground drift. The seismic data set consists of P- and S-wave traveltimes and amplitudes measured along 162 raypaths between two boreholes. Eighteen sources were located at 0.5 m intervals in a 10 m borehole, and nine geophones at 1.0 m intervals were located in a parallel borehole approximately 4 m away, as shown in Figure 2. This study used two suites of measurements, the first taken after the heater had been turned on for several weeks and the second several days after the heater had been turned off. The objective was to determine how well the reconstructions could detect slowness or attenuation changes due to heat-induced changes in stresses and fractures. The geometry of the experiment is conventional crosshole, so that the range of angles through the area of interest is limited, though reasonable (−66 degrees to +66 degrees at the heater location), and the sampling was at regular intervals. The data were collected with high accuracy. Source and receiver locations were measured to 1.0 mm and traveltimes were read to 1.0 μs.

METHOD

The region encompassed by these sources and receivers is represented by a two-dimensional (2-D) area for which the velocity or attenuation distribution is to be determined. The method of processing is based on the relation between propagation velocity and the total traveltime, or between attenuation characteristics and received amplitude, for a particular raypath in the x-y plane. For total traveltime this relation is

$$t_k = \int_{R_k} \frac{da}{v(x, y)}, \tag{1}$$

where $v(x, y)$ is the velocity of the medium and the integration is along the particular raypath R_k. The amplitude A_k is related to the attenuation field $\alpha(x, y)$ through the equation

$$A_k = A_0 \exp\left[-\int_{R_k} \alpha(x, y)\, ds \right],$$

where $\alpha(x, y) = \pi f/cQ$ and c and Q are dependent upon (x, y). A_0 has been corrected for the radiation pattern, geometric

spreading, and instrument response. $\alpha(x, y)$ describes only the effects of apparent attenuation, i.e., intrinsic dissipation and elastic scattering. The projection is then defined as

$$P_k = \ln \frac{A_k}{A_0} = -\int_{R_k} \alpha(x, y)\, ds,$$

where A_k is the received amplitude and A_0 is the source amplitude. In general, the integral equation is written

$$y_k = \int_{R_k} x(r, s)\, da \tag{2}$$

with y_k, $k = 1, 2, \ldots, N$ representing the measured traveltime or amplitude for N paths and x representing the slowness or attenuation operator. After discretizing the field, the line integral becomes a finite sum and the problem may be described by a set of linear equations

$$y_k = \sum_{i=1}^{I} \Delta a_{ki} x_i, \qquad k = 1, 2, \ldots, N, \tag{3}$$

where Δa_{ki} is the length of the ray k which penetrates pixel i, I is the total number of pixels intersected by the ray k, and x_i is the property of pixel i.

In matrix notation, this is written $\mathbf{y} = \underline{\mathbf{A}}\mathbf{x}$. Through common inversion techniques, the equation may in principle be solved for $\mathbf{x}$. Due to the large, sparse arrays involved, this is usually impractical. Sparse matrices have been well-studied in linear algebra, and the techniques developed have been applied to tomography in ART. These techniques are iterative, i.e., where one equation (one raypath) is analyzed at a time. The algorithms require an initial slowness solution $\mathbf{x}^0$ usually found by a simple back-projection of the data or by specifying a reasonable model. An estimate for y_k^n is calculated along each raypath,

$$\bar{y}_k^n = \sum_{i=1}^{I} \Delta a_{ki} x_i^n, \tag{4}$$

where x^n indicates the estimated slowness after the nth iteration. A single iteration includes an analysis of all sets of rays. Most algorithms are based on some minimization of the residual error Δy_k, which is the difference between the observed data y_k and the calculated data $\bar{y}_k$

$$\Delta y_k^n = (y_k - \bar{y}_k^n) = \sum_{i=1}^{I} \Delta a_{ki} \Delta x_i^n, \tag{5}$$

where Δx_i^n form the set of corrections to the previous slowness values. Determination of this correction is the basis of ART algorithms. The correction is then applied to each pixel through which the ray k passes,

$$x_i^{n+1} = x_i^n + \Delta x_{ki}^{n+1}. \tag{6}$$

Alternatively, the correlations may be applied after all N rays have been analyzed by averaging the corrections of each single pixel

$$\Delta x_i^n = \frac{1}{M_i} \sum_{k=1}^{N} \Delta x_{ki}^n, \tag{7}$$

where M_i is the number of rays passing through cell i.

ART was initially used as a reconstruction algorithm in Gordon et al. (1970) and was later found to be similar to algorithms already used in mathematics for solving systems of

400 METERS

320 METERS

NO. OF RAYS

1—15
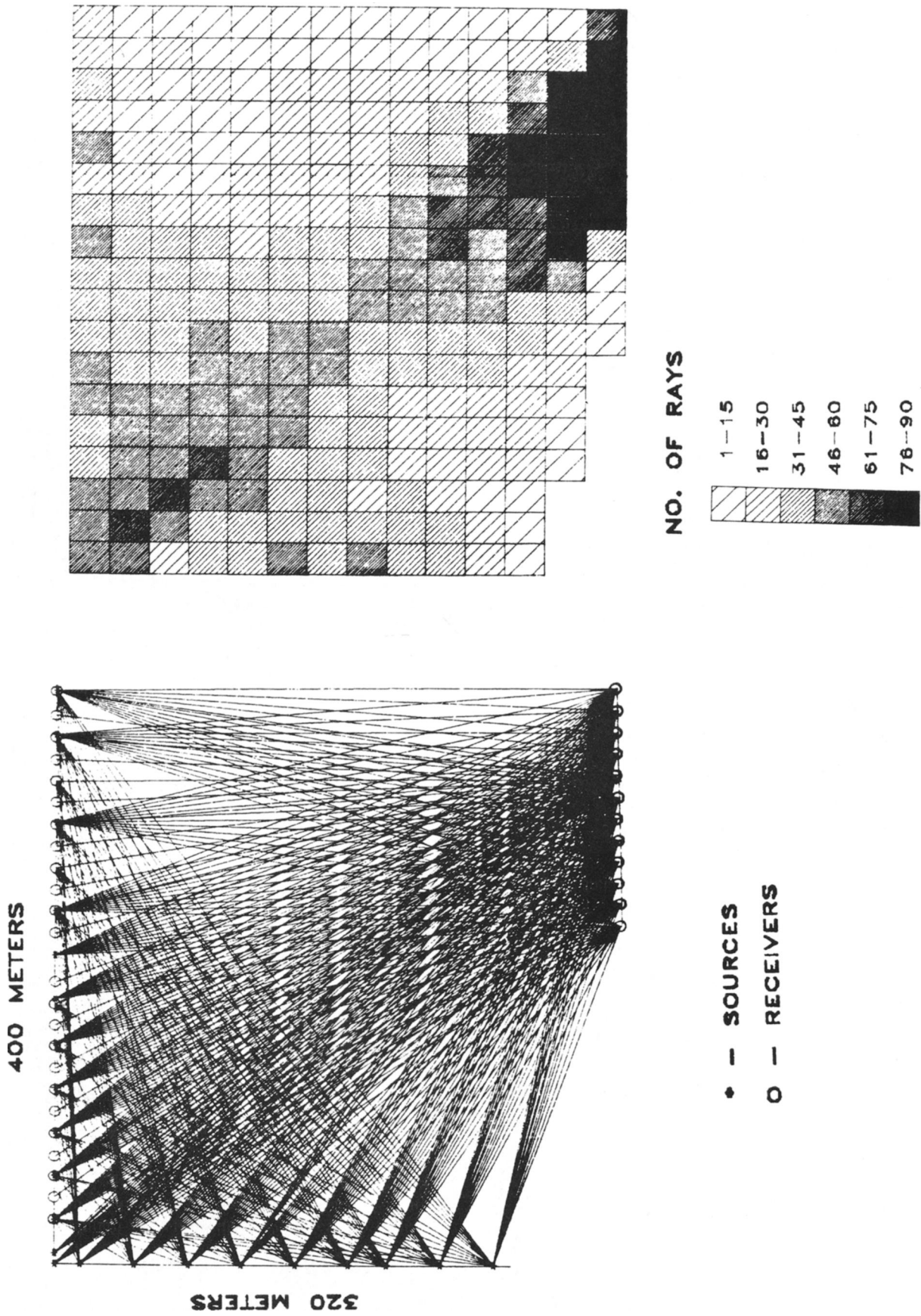16—30
31—45
46—60
61—75
76—90

• — SOURCES

○ — RECEIVERS

FIG. 1. (a) The raypaths for the Retsoff data showing arrays on the surface, in the borehole to the left and in the mine at the bottom. (b) The ray density for each pixel. Darker rays represent greater sampling. The sampling is dominated by paths from the mine to the upper left of the plot.

NO. OF RAYS

	1— 8
	9—15
	16—23
	24—30
	31—38
	39—45

4.2 METERS
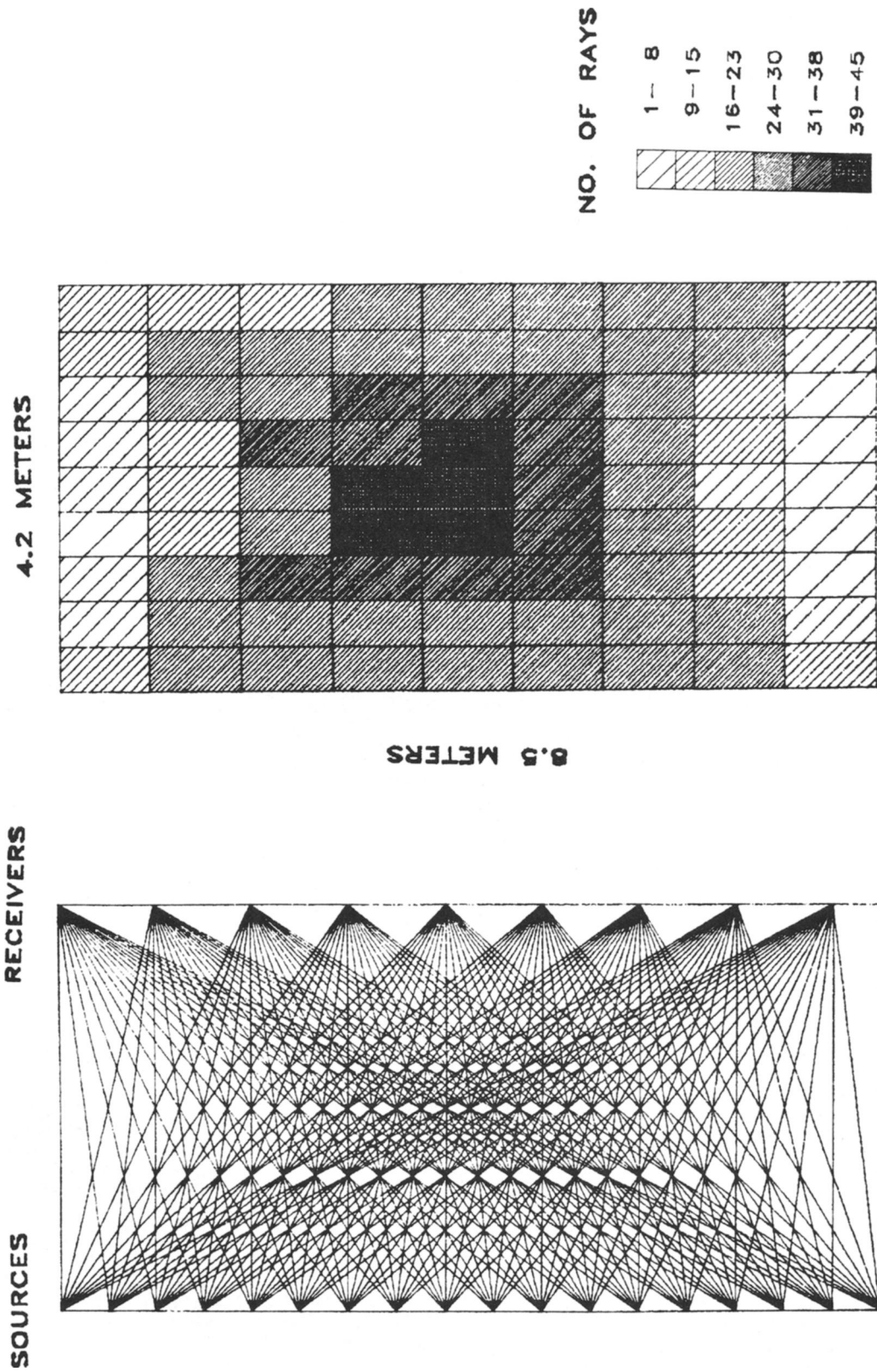
8.5 METERS

RECEIVERS

SOURCES

FIG. 2. (a) The raypaths for the Stripa data, and (b) the ray density for each pixel. This geometry provides high symmetry in the sampling.

linear equations. Several such algorithms are described in the following sections.

Algorithm 1. ART

$$x_i^{n+1} = x_i^n + \frac{\Delta y_k^n}{\sum\limits_{i=1}^{I} \Delta a_{ki}^2} \Delta a_{ki}, \qquad k = 1, 2, \ldots, N. \qquad (8)$$

The right term is the correction term Δx_{ki}^n. Dines and Lytle (1979) used a least-squares minimization in their derivation of algorithm 1. They also gave the minimax corrections obtained by minimizing the L^∞ norm which gives algorithm 2, ART 1.

Algorithm 2. ART1

$$x_i^{n+1} = x_i^n + \frac{\text{sgn } (\Delta a_{ki})\Delta y_k^n}{\sum\limits_{i=1}^{I} |\Delta a_{ki}|}, \qquad k = 1, 2, \ldots, N, \qquad (9)$$

where sgn is the signum function which in this case is always equal to 1.0 since Δa_{ki} is length and, therefore, always positive. This is just a simple back-projection; the same value is added to all cells regardless of the length of ray segment which intersects the pixel. Note also that the denominator is just the total length of the raypath. The advantage of ART1 is that the segment lengths Δa_{ki} can be ignored, reducing the necessary storage space and computation time. Only the ray length and those cells through which the ray passes are needed.

In practical implementation of ART, relaxation parameters become extremely important. This is a sequence of numbers λ_k usually confined to the interval $0 \leq \lambda_k \leq 2$ which typically appear in ART as

$$x_i^{n+1} = x_i^k + \lambda_k \frac{\Delta y_k^n}{\sum\limits_{i=1}^{I} \Delta a_{ki}^2} \Delta a_{ki}, \qquad k = 1, 2, \ldots, N \qquad (10)$$

and which allows control of the rate of convergence (Herman et al., 1978).

The problem may be approached in terms of entropy optimization (Gordon et al., 1970). This refers to the mathematical problem of maximizing the functional

$$f(x) = -\sum\limits_{j=1}^{m} x_j \ln x_j \qquad (11)$$

over various sets of constraints. In the present case the constraints would be the collected data in the form of equation (1) and the a priori information that slowness is positive, $x_i \geq 0$. As seen from algorithm 3 below, the corrections are multiplied by, rather than added to, the previous slowness field, leading to the term multiplicative algebraic reconstruction technique (MART).

Algorithm 3. MART

$$x_i^{n+1} = \left(\frac{y_k^n}{\sum\limits_{i=1}^{I} \Delta a_{ki} x_i} \right)^{\lambda_k \Delta a_{ki}} x_i^n. \qquad (12)$$

Here the λ_k are relaxation parameters such that $0 \leq \lambda_k \leq 1$. Note that they are no longer dimensionless but have the dimension $(\text{length})^{-1}$ which becomes very important when determining their values. To be mathematically complete, the slowness field x^0 must be initialized as e^{-1} where e is the base

of the natural logarithms. The behavior of this algorithm in practical situations in the presence of noise is completely unknown.

PRACTICAL CONSIDERATIONS

In seismological applications, noise and irregular geometry cause the equations to be inconsistent. Noise may be due to measurement errors of both traveltime and source/receiver locations, while irregular geometry results in limited angular coverage, highly curved rays, or incomplete projections. ART still tries to satisfy these equations exactly and the resulting reconstruction may be far from the actual picture. Measurement errors cannot be avoided and it must be assumed that the problem is stable enough for a satisfactory solution to be found.

In practice, crosshole seismic measurements are limited to a few directions with nonuniform sampling. Use of convolution or Fourier methods requires interpolation to complete the projections and angular coverage. ART methods treat each ray as an equation; hence a missing ray or penetration angle becomes a missing equation which can be ignored. Sparse sampling, however, results in "smearing" of the zones of anomalous slowness. This was shown in McMechan (1983) for synthetic data and in Menke (1984) in a calculated resolution matrix. They show that, for a parallel borehole configuration, vertical slowness variations are well resolved, but horizontal variations are smeared across the field.

Another cause of smearing is variation in raypath length. Depending upon the geometry, some short paths may sample only one pixel, while others may intersect many. In the above algorithms, both raypaths would have equal weight in the correction term for that one pixel. Intuitively, it is reasonable that a greater weight should be given to the short ray than to the long ray which is affected by many different pixel slownesses. Without some weighting scheme, longer rays tend to dominate, smearing any zones of anomalous slowness. Unfortunately, there is no mathematically correct way to determine an optimal weighting scheme, and so one must be found experimentally. The weights are applied to the corrections after each ray is analyzed:

$$x_i^{n+1} = x_i^n + W_{ki}\Delta x_{ki}^n, \qquad k = 1, 2, \ldots, N. \qquad (13)$$

Two weighting schemes were found to give some improvement of image quality. The first scheme weights according to the ratio of cell width to path length.

$$W_{ki} = \left(\frac{C}{\sum\limits_{i=1}^{I} \Delta a_{kl}} \right)^4, \qquad (14)$$

where C is the cell width and the denominator the path length. The second scheme weights according to the ratio of the length of path through the cell to the total path length

$$W_{ki} = \frac{\Delta a_{ki}}{\sum\limits_{i=1}^{I} \Delta a_{ki}}. \qquad (15)$$

These weighting schemes were developed empirically and other schemes may prove more suitable.

The presence of variations in velocity of attenuation leads to raypaths which violate the assumption of straight raypaths.

Depending upon the size of the velocity contrasts, the Fermat path curves to a certain degree. The flexibility of the ART algorithms allows these curved paths to be incorporated through ray tracing. Preliminary application to the Stripa data sets shows little improvement, indicating the straight-ray assumption is reasonable, at least in the case of that data set.

In this study the two typical data sets were used to study the performance and sensitivities of the various algorithms for various weighting and relaxation parameters. Characterizing performance is difficult in that it requires measurement of convergence rate and solution quality or reliability.

CONVERGENCE AND RELIABILITY

The data from the Retsoff and Stripa sites were processed using the above algorithms. In an effort to assess the relative reliability of the different algorithms and to determine the optimal relaxation parameter and weighting schemes for each, several weights and relaxation values were used with each algorithm. Problems arise from the ambiguity of the solution and the fact that, although these methods initially converge to a plausible solution, they eventually diverge after a number of iterations (Herman et al., 1973). Most authors have used convergence criteria and reliability measurements for test data, based on knowledge of the correct solution. In a real experiment, the actual structure and therefore the correct solution, is unknown. Those who have addressed these problems with real data have not developed any rigid criteria by which to test the solution. Measures of reliability and resolution are either made by visual inspection or by single statistical values such as variance.

Three mathematical measures have been used to measure reliability and resolution and to determine stopping criteria (Gordon et al.; Herman, 1970): the distance between the measured and calculated projection values (discrepancy)

$$D^n = \sqrt{\frac{1}{N} \sum_{k=1}^{N} (\Delta y_k^2)}, \tag{16}$$

the variance

$$V_n = \frac{1}{I} \sum_{i=1}^{I} (x_i^n - \bar{x})^2, \tag{17}$$

where $\bar{x}$ is the mean slowness of the field; the entropy is

$$S^n = \frac{-1}{\ln n} \sum_{i=1}^{I} \left(\frac{x_i^n}{\bar{x}}\right) \ln \left(\frac{x_i^n}{\bar{x}}\right). \tag{18}$$

If the set of equations (3) is complete and consistent, D^n will tend to zero while V^n will tend to minima and S^n to maxima with increasing n. The purpose of minimizing variance (or maximizing entropy) is to find the "smoothest" possible image, i.e., the one closest to mean which still satisfies the data. In real applications the starting model is often excessively smooth, so that the variance actually increases (and the entropy decreases) to satisfy the data. D^n, V^n, and S^n measure convergence to the solution, but not closeness of the solution to the true image. In fact, these measures may continue to "converge" while the solution diverges unacceptably from the true image, and some stopping criterion is needed.

Visual inspection as a stopping criterion is completely subjective. One such visual measure used initially was the amount of oscillation observed between adjacent pixels. This phenom-

enon is caused by overshooting the solution, particularly for poorly determined problems, and it may be controlled by decreasing the relaxation parameter or the number of iterations. Oscillation in the solution may be measured by its 2-D spatial Fourier transform. In wavenumber space, the oscillations appear as large amplitudes at values of C^{-1}, where C is the pixel width. Generally, the smoother the Fourier transform, the less oscillation is present in the solution.

Other visual measures check for large deviations from plausible models, both in location of the anomalous zones and the actual velocity values in the field. The true velocity field is unknown, but often something is known about the range of velocities expected and the general locations of expected low- and high-velocity zones. If no such information is available for the area of interest, or if an unexpected feature is obtained, a more systematic procedure may be followed to ensure that the feature is real (Gordon, 1974). The method essentially measures the sensitivity of the solution to the starting model x_i^0. There may be some consistent features among solutions while others appear only for a few starting models and thus are suspect. Another procedure consists in changing the values of anomalous zones in a solution and then using this model as the initial slowness field in a new iteration. If the zone does not appear in the new reconstruction, its significance is questionable. If it does remain, some confidence is gained about its accuracy since its presence apparently is required by the data.

The sequence of checks used in this study began with a visual evaluation of the velocity anomalies and the amplitude of oscillation between pixels. Usually, the expected general features appeared in the final image, but adjacent cell velocities varied excessively. The value of the relaxation parameter was adjusted until satisfactory smoothness (by visual standards) was achieved. After an acceptable relaxation was achieved, the resulting features could be analyzed. The mathematical measures were useful in determining the optimal number of iterations and in comparing the different algorithms and weighting schemes.

RESULTS

Six different algorithms and weighting schemes were used to analyze the two data sets. These include

ART—given as algorithm 1, equation (8),
ART1—given as algorithm 2, equation (9),
MART—given as algorithm 3, equation (12),
WART—applying weighting scheme 1, equation (14), to ART,
WARTA—applying weighting scheme 2, equation (15), to ART, and
WART1A—applying weighting scheme 2, equation (15), to ART1.

For each of these algorithms the image was corrected after each ray was analyzed. For these same algorithms the image was also corrected using equation (7) (specified by an "a," e.g., ARTa). This gives a total of twelve methods for comparison. In general, determining the proper relaxation parameter and stopping criterion for reasonable solutions required considerable experience and manipulation.

The Retsoff data set is an example of very noisy data; the sources and receivers do not lie in a plane, the dimensions are

fairly large (hundreds of meters), the traveltimes must be corrected for topography, the range of projection angles through each cell is limited, the ray lengths are highly variable, and the velocity contrasts can be rather large and cause problems with curved rays. The raypath configuration is shown in Figure 1a, with the number of rays through each box depicted in Figure 1b. The drawbacks to the geometry are easily seen in Figure 1b; there are areas of very low-density and very high-density coverage, with poor angular coverage in some areas and with many almost redundant rays. A swath of reasonable coverage with rays penetrating from many directions runs from the mine toward the borehole-surface intersection (lower right to upper left in the figure).

The area of interest was divided into an 18 × 14 field of pixels ($I = 252$) giving a cell dimension of about 25 m on a side. Smaller cells may be used to increase resolution, but the nature of the Retsoff data leads to large oscillations in slowness between cells because the solution is becoming increasingly underdetermined. Despite the inconsistencies in the data, the reconstruction was successful. Figure 3 shows the velocity field determined by each of the twelve variations on the algorithms, with their respective k-k plots.

The various solutions differ in detail, but two general features are consistent in all the reconstructions. There is a very low-velocity zone (about 2.75 km/s) at the base of the field below a V-shaped zone of intermediate velocities (4.00 km/s); this low-velocity field is bounded by two zones in which velocity increases with depth. These features, which show velocity contrasts as high as 40 percent, are consistent with results from other studies of the area. The solutions oscillate similarly as seen in the k-k analyses. The k-k plots indicate that most of the velocity variation seen is in the low-

wavenumber region (upper left-hand corner) and virtually no short-wavelength oscillation (high k_x) in the horizontal direction. The only real differences in the different reconstructions are in the high k_z direction (short-wavelength oscillations in the vertical direction) where the weighted algorithms produce solutions with lower oscillation noise. Most oscillations occur in areas of low ray density or low angular coverage toward the upper right and lower left of the figure.

On applying the algorithms to these data, the relaxation parameters were used to control the rate of convergence so that the optimal reconstruction occurred after about six iterations. The convergence of some of the weighted algorithms was very slow, so a high damping was used along with a greater number of iterations, e.g., WARTAa in Table 1, where $\lambda = 2.00$. The convergence criteria and residuals given in Table 1 show small differences among the various algorithms. Based on these values, one algorithm cannot be deemed better than another, because the algorithm with the lowest variance is not necessarily the one with the lowest discrepancy, and vice versa. For example, WART has the lowest variance, while it also exhibits a high discrepancy. In general, the discrepancy D^n initially decreased very quickly, leveling off after a few iterations. Similarly, the variance V^n quickly increased, then leveled off. Synthetic data have shown that the optimal image occurs just as these parameters level off.

The Stripa data represented generally a much "cleaner" data set than the Retsoff data; the measurements were very accurate, the dimensions of the experiment were small, the ray lengths are similar, and the velocity contrasts are very small, with only 300–400 m/s separating the highest and lowest values. As shown in Figure 2, the region was divided into a 9 × 9 field of rectangular pixels giving 81 1.0 × 0.5 m pixels.

Table 1. Parameters resulting from reconstruction of the Retsoff data. The variance V^n, the discrepancy D^n and the relaxation parameter λ are described in the text. "Max" and "min" are the maximum and minimum velocities found in the resulting reconstructed image.

| RETSOFF SALT MINE						
Algorithm	Variance (s^2/ km^2)	Discrepancy (sec)	Iter	λ	Max (km/s)	Min (km/s)
ART	6.151×10^{-2}	7.48×10^{-2}	4	0.04	1.80	0.91
ARTa	6.137×10^{-2}	8.60×10^{-2}	7	0.50	1.82	1.08
ART1	6.154×10^{-2}	7.61×10^{-2}	6	0.02	1.80	0.90
ART1a	6.132×10^{-2}	8.57×10^{-2}	6	0.50	1.83	1.08
MART	6.156×10^{-2}	7.29×10^{-2}	5	0.0005	1.80	0.83
MARTa	6.137×10^{-2}	8.58×10^{-2}	5	0.01	1.81	1.05
WART	6.111×10^{-2}	8.76×10^{-2}	7	0.30	1.66	1.05
WARTa	6.101×10^{-2}	9.64×10^{-2}	20	2.00	1.64	1.15
WARTA	6.140×10^{-2}	7.70×10^{-2}	6	0.30	1.74	0.98
WARTAa	6.127×10^{-2}	8.96×10^{-2}	20	2.00	1.74	1.13
WART1A	6.143×10^{-2}	7.48×10^{-2}	4	0.50	1.75	0.96
WART1Aa	6.125×10^{-2}	8.97×10^{-2}	20	2.00	1.73	1.14
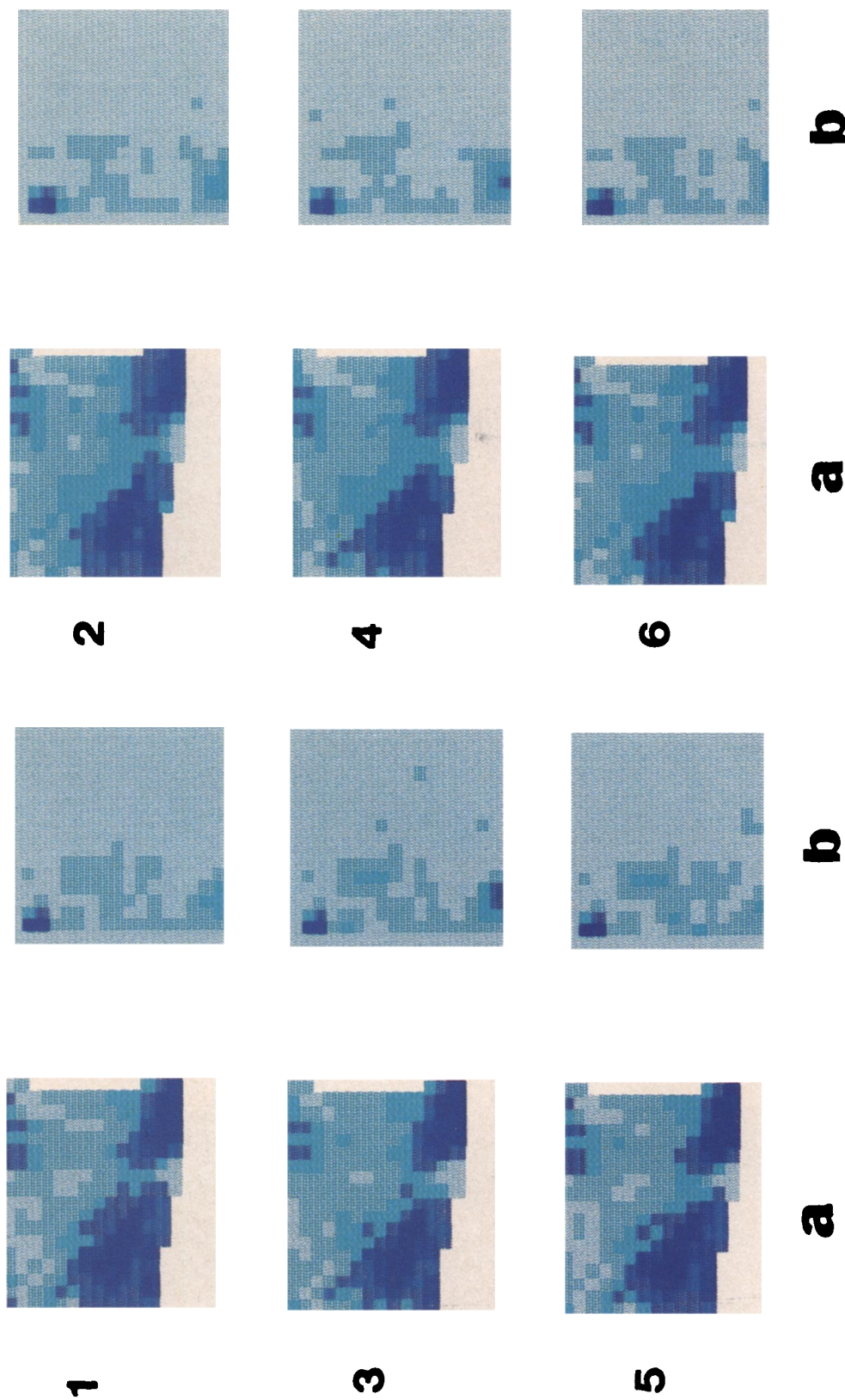
FIG. 3. (a) Compressional velocity field for the Retsoff data and (b) the corresponding $k_x - k_z$ plots. For (a) the geometry is the same as in Figure 1 and the darker blues correspond to higher velocities. The origin in (b) is to the upper left with the horizontal wavenumber (k_x) increasing to the right to a value of 0.02 m^{-1} and the vertical wavenumber (k_z) increasing downward to the same value. The darker blues correspond to higher amplitudes, showing that most of the energy is in the longer wavelengths and low-oscillating images will have small amplitudes at the higher ends of the spectrum. The algorithms are: (1) ART, (2) ARTa, (3) ART1, (4) ART1a, (5) MART, (6) MARTa, (7) WART, (8) WARTa, (9) WARTa, (10) WARTAa, (11) WART1A, (12) WART1Aa.
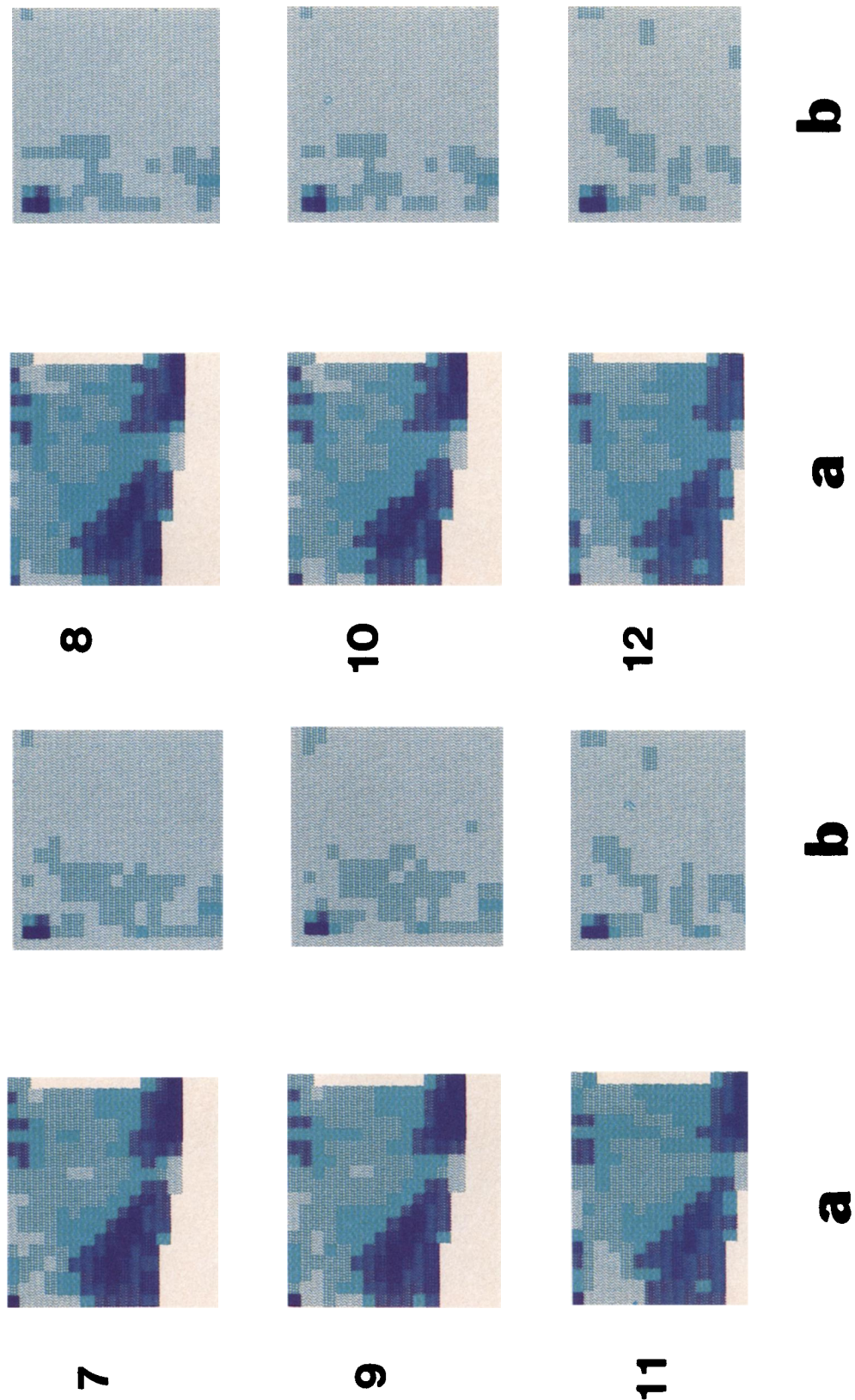
RETSOFF

7   a   b   8   a   b

9   a   b   10   a   b

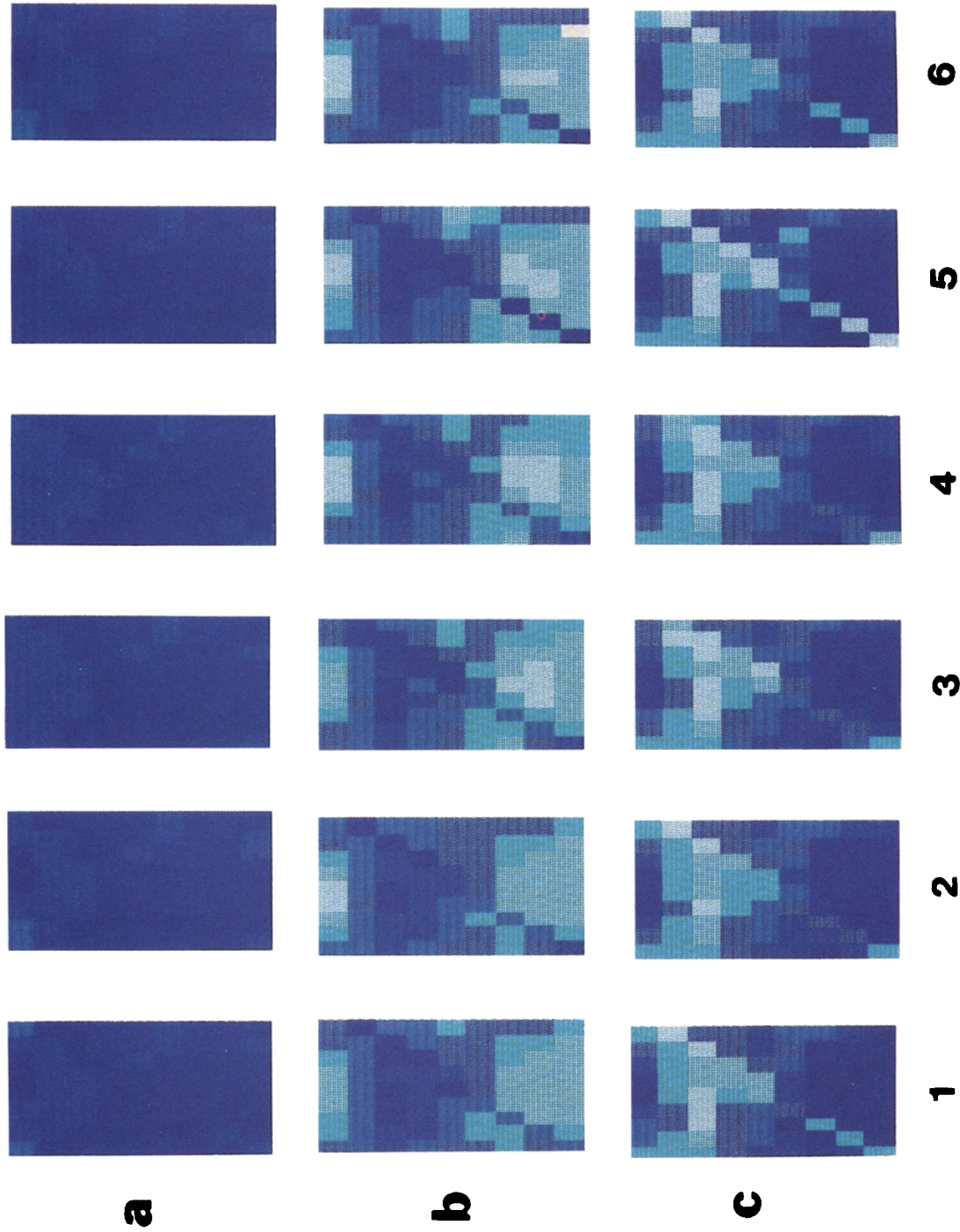11   a   b   12   a   b

FIG. 3b.

S T R I P A

FIG. 4. Compressional velocity field for the Stripa data for the same algorithms as in Figure 3 and the same geometry as Figure 2. The darker blues correspond to higher velocities in (a) and (c) and larger velocity differences in (b). (a) The velocity field during heating, (b) the difference in velocities between (a) and (c). (c) The velocity field after cooling.
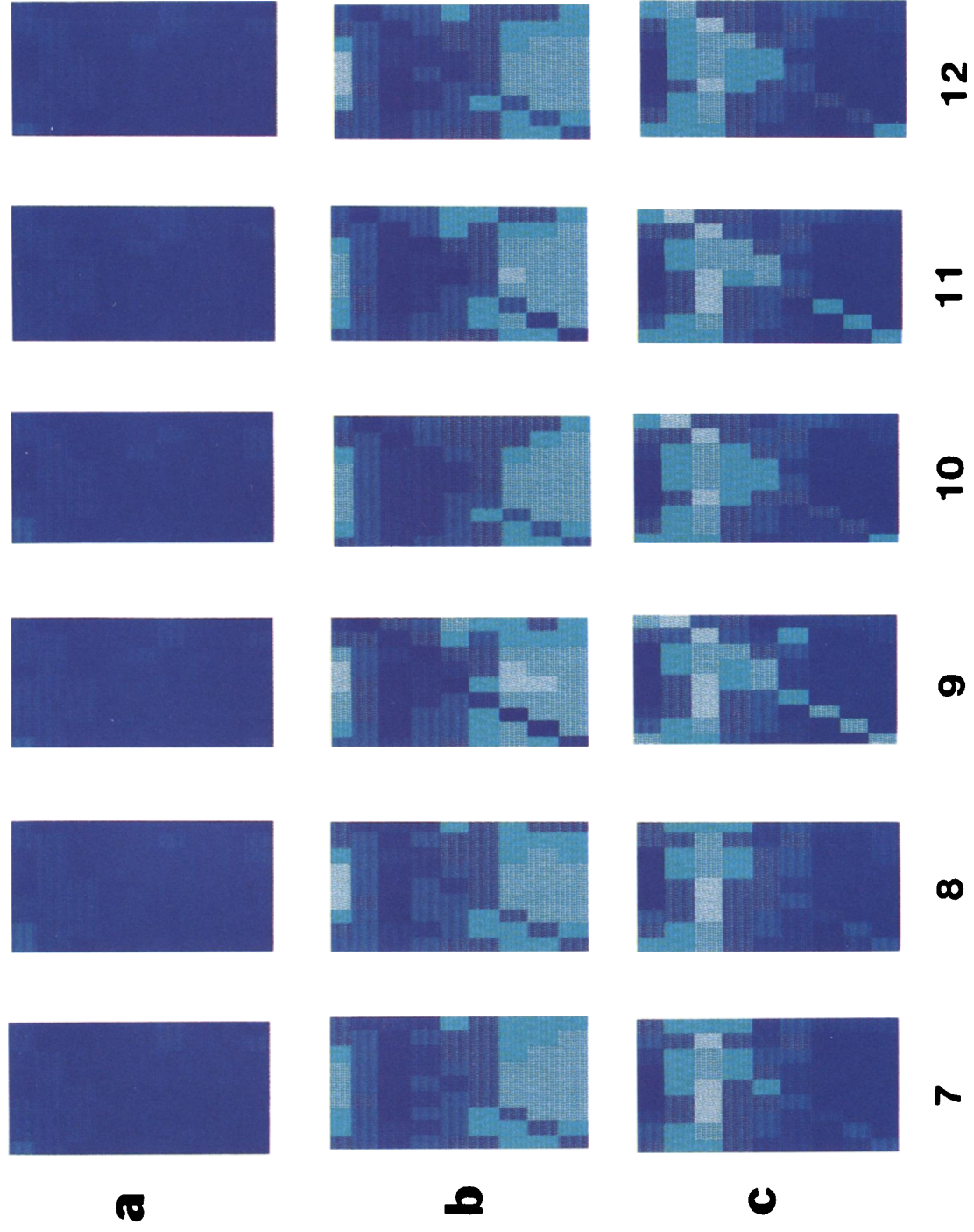
FIG. 4b.

The 1 m separation between receiver locations limits the minimum cell dimension. A finer vertical division decreases the number of rays per cell, giving many unsampled pixels near the edges. The coverage is vertically symmetric about the center line and much more structured than the Retsoff survey, as would be expected from a small-scale borehole experiment. The ray density was greatest toward the center of the region where the angular range of sampling is as much as 130 degrees. The small diamond-shaped holes in the ray coverage are insignificant with respect to the pixel size.

These high-quality data lead to a more stable solution, i.e., a similar solution is obtained from all methods applied to a common starting model. More detail is recovered, and consistent solutions are obtained if even half the rays are ignored. Figure 4 shows plots of the velocity fields at full heating and after heater deactivation. Wavenumber spectrum calculations were not performed due to the limited length of the image (dimension 9 × 9). Solutions from the various algorithms are all quite similar. While the heater was on, a rather constant velocity field of about 5.95 km/s was maintained (Figure 4a). After the heat source was removed, a low-velocity zone of 5.6–5.7 km/s developed in the location of the heat source and extended to the upper right of the section. Some smearing of this zone takes place, especially on a diagonal extending from the lower left corner toward the upper right. The weighted algorithms (especially WART) partially reduce this effect. Table 2 shows the consistencies of the algorithms with small differences seen between the variances and the discrepancies. It also shows that data set 1 (Table 2a) with virtually no velocity contrasts gives much smaller residuals.

DISCUSSION

Two data sets were analyzed using various ART algorithms to compare the performances of these techniques in processing real geophysical data sets of good and average quality. The reconstructions of both data sets are quite consistent with known structures and expected velocity fields. In the Retsoff mine experiment, the important features revealed in the reconstruction are the V-shaped low-velocity zone through the center of the picture, the extremely low velocities at the collapsed end of the mine, and the general increase in velocity with depth, from about 4.00 to 5.5 km/s, equivalent probably to the velocity field before the collapse and alteration. This represents up to a 40 percent velocity contrast. The large low-velocity zone is interpreted as being due to groundwater flow and resulting alteration and dissolution of the carbonate rocks. This low-velocity zone intersects the mine where major alteration and collapse of material into the mine is occurring. Problems with the reconstruction include some smearing to the lower left of the picture and an anomalous high-velocity zone at the upper right, both of which may be due to poor coverage and resulting oscillations in the data. In general, the reconstruction gives a fairly detailed picture of what is happening in the section.

The Stripa experiment was conducted to study the effects of increased temperature on a granitic rock mass from emplacement of radioactive waste cannisters in boreholes in an underground repository. Measurements were taken during and after emplacement of an equivalent electrical heater. The fairly uniform velocity seen during heating (Figure 4) is apparently due to the closure of fractures by thermal expansion (King and Paulsson, 1981). Velocities decreased upon heater removal due to the opening of fractures, giving a maximum velocity contrast of about 8 percent. Some permanent damage (thermal fracturing) was seen in the central region where the heat was greatest and where previous calcite fracturing was evident. The diagonal line of low velocity extending from bottom left to upper right is possibly due to numerical streaking of low velocities created by calcite fracturing at its upper right terminus and drilling damage at the bottom of borehole M6. This is suggested from fracture mapping and the existence of low-velocity zones in these areas even during heating. Horizontal extension of the central low-velocity zone to the sides of the figure is evident, as seen in the studies by Menke (1984) and McMechan (1983). Some of the problems of ART are seen in this reconstruction, but a reasonably accurate picture of the change in velocity field is achieved.

The performance of the ART algorithms used depends upon the data set, differing even between the two Stripa data sets. Accuracy of measurements, pixel size, ray density, angular coverage, and velocity contrast all affect the algorithms. To characterize performance for purposes of comparison, we rely primarily on visual appearance with the help of k-k plots, when applicable, and on the plausibility of the results, given other knowledge of properties of the media. The convergence criteria were considered secondarily. In general, all the algorithms give consistent, apparently reliable reconstructions and any of them could be recommended. Correcting the image after each ray is analyzed seems preferable over the averaging method of equation (7), due primarily to the averaging of high-velocity contrasts into high-wavenumber (short-wavelength) oscillation as seen in the k-k plots. These wavenumber plots show that all the nonweighted algorithms have high-wavenumber oscillation, while the weighting almost eliminates this. The weighted algorithms (WART and WARTA) are also superior in the lower residuals produced.

The largest expected problem is in the straight-ray assumption, given curved raypaths due to the velocity contrasts (up to 40 percent for the Retsoff data). While some image distortion inevitably occurs, it is not a substantial problem. The low-velocity zones at both Stripa and Retsoff are determined to the size of the pixels in the analysis. This is not to say that a curved-ray algorithm should not be developed, since more detailed studies will eventually need such a capacity. Most of the image distortion is caused by incomplete data in the form of low ray density and, more importantly, incomplete angular coverage. Optimizing the experiment in terms of source and receiver locations reduces these problems. Sometimes this may be difficult, but the "filling in" of a few essential rays often justifies the effort in terms of resolution. An optimal configuration would be similar to that of Retsoff in that the region is almost surrounded by sources. Addition of sources or receivers down a borehole or shaft at the right of the picture improves the geometry. The Stripa experiment used the more classic crosshole situation of parallel boreholes. Greater resolution, especially toward the top of the region, could have been achieved with a line of surface receivers to increase the angular coverage and determine better the horizontal extent of the low-velocity zone (see Menke, 1984; McMechan, 1983).

Further information may be obtained by using ART on amplitude data and S-wave traveltimes. S-waves are analyzed in the same manner as P-waves. Reading errors for S-waves

Table 2. Parameters, as defined in Table 1, resulting from reconstruction of the Stripa data (a) while the heater was turned on, and (b) after the rock had cooled.

STRIPA - DATA SET 1						
Algorithm	Variance (s^2/km^2)	Discrepancy (sec)	Iter	λ	Max (km/s)	Min (km/s)
ART	2.434×10^{-2}	5.67×10^{-3}	2	0.10	6.04	5.941
ARTa	2.435×10^{-2}	5.74×10^{-3}	6	0.50	6.03	5.936
ART1	2.443×10^{-2}	6.57×10^{-3}	5	0.01	6.01	5.947
ART1a	2.444×10^{-2}	7.77×10^{-3}	3	0.20	6.00	5.946
MART	2.437×10^{-2}	2.02×10^{-2}	7	0.03	6.03	5.935
MARTa	2.435×10^{-2}	1.95×10^{-2}	6	1.00	6.03	5.934
WART	2.433×10^{-2}	6.07×10^{-3}	4	0.07	6.03	5.945
WARTa	2.433×10^{-2}	6.03×10^{-3}	5	1.00	6.03	5.946
WARTA	2.436×10^{-2}	5.81×10^{-3}	6	0.20	6.03	5.934
WARTAa	2.435×10^{-2}	5.78×10^{-3}	20	1.50	6.02	5.934
WART1A	2.436×10^{-2}	5.87×10^{-3}	4	0.30	6.03	5.938
WART1Aa	2.436×10^{-2}	6.13×10^{-3}	15	1.50	6.02	5.940

(a)

STRIPA - DATA SET 2						
Algorithm	Variance (s^2/km^2)	Discrepancy (sec)	Iter	λ	Max (km/s)	Min (km/s)
ART	2.507×10^{-2}	1.23×10^{-2}	3	0.07	6.07	5.654
ARTa	2.506×10^{-2}	1.30×10^{-2}	5	0.70	6.04	5.719
ART1	2.508×10^{-2}	1.30×10^{-2}	5	0.05	6.05	5.707
ART1a	2.505×10^{-2}	4.05×10^{-2}	5	1.00	6.06	5.722
MART	2.506×10^{-2}	4.20×10^{-2}	8	0.10	6.07	5.615
MARTa	2.506×10^{-2}	1.44×10^{-2}	9	1.00	6.05	5.680
WART	2.497×10^{-2}	1.44×10^{-2}	4	0.10	6.04	5.751
WARTa	2.497×10^{-2}	1.39×10^{-2}	9	1.00	6.05	5.753
WARTA	2.504×10^{-2}	1.16×10^{-2}	6	0.70	6.07	5.622
WARTAa	2.506×10^{-2}	1.33×10^{-2}	20	1.50	6.03	5.725
WART1A	2.505×10^{-2}	1.23×10^{-2}	6	0.50	6.06	5.677
WART1Aa	2.504×10^{-2}	1.30×10^{-2}	20	2.00	6.04	5.722

(b)

SHEAR WAVE VELOCITIES

VELOCITY DIFFERENCE

STRIPA

DURING HEATING

AFTER COOLING

velocity (km/s)

3.25   3.5
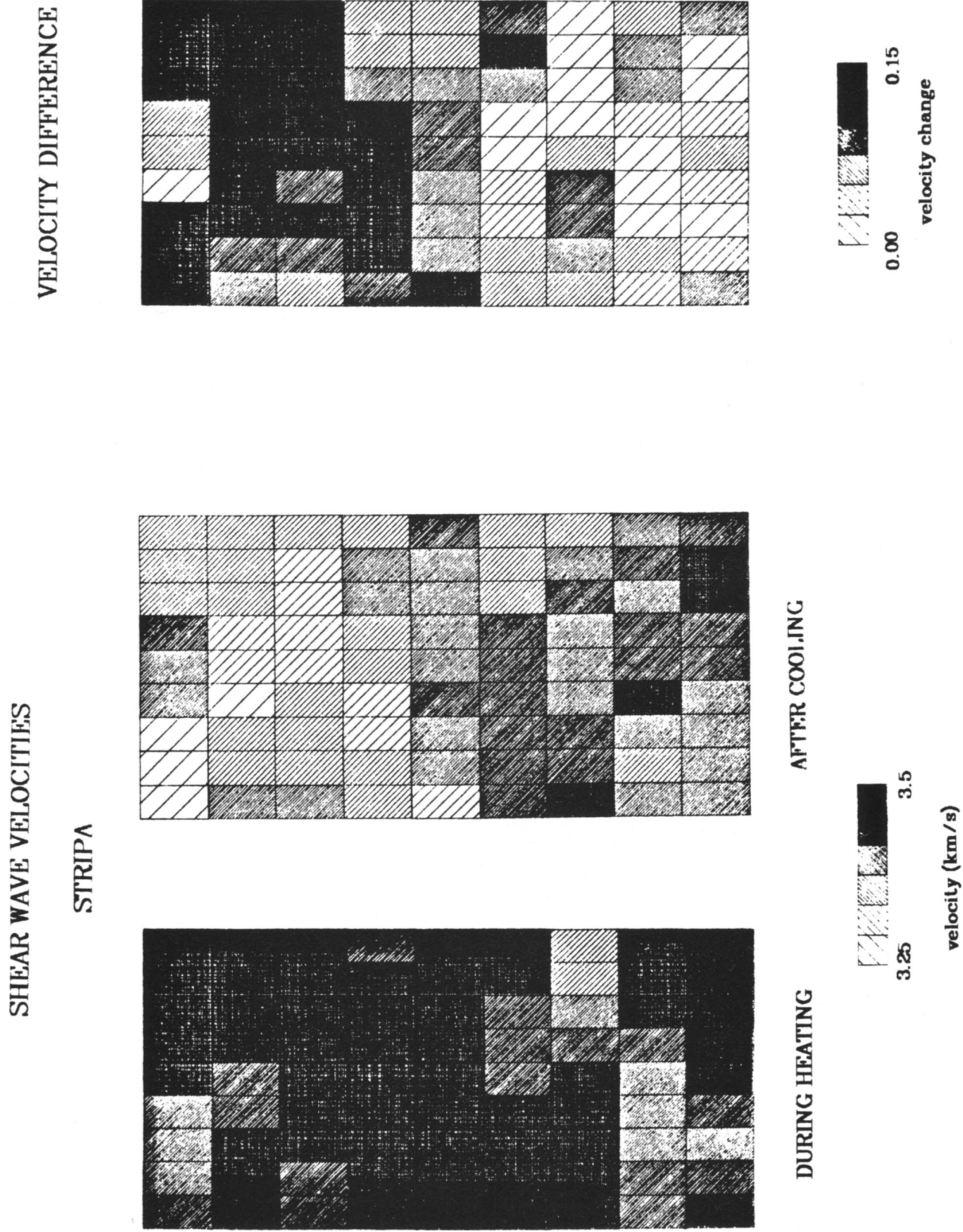
velocity change

0.00   0.15

FIG. 5. An example of the shear velocity field for the Stripa data during heating and after cooling using the WARTa algorithm. The figure to the right shows the differences in velocity as in Figure 4b.

are inherently larger than for P-waves, leading to a noisier, oscillating solution. However, this effect is mitigated somewhat by the slower velocities and longer traveltime, and tends to reduce the fractional time error. An example from the Stripa S-wave data is shown in Figure 5. The reconstruction is noisier than for the P-waves, but the same basic image is reconstructed except for local differences such as the low-velocity zone to the lower right during heating. Amplitudes describe the field of attenuation properties. In fact, tomography in other fields is usually applied to amplitude data. The same algorithms are used, though the problem is set up slightly differently [see equation (2)]. Amplitudes are more difficult to use in seismology, because they require identical or accurately normalized sources (see Wong et al., 1983). Variation in amplitudes is caused not only by changes in the loss properties, but also by scattering, refraction, reflection, and the distortion of the wave field due to curvature of raypaths.

CONCLUSION

ART-type algorithms have been shown, with real data, to offer a rapid, reliable means of reconstructing the slowness field. Details in the form of low-velocity zones in media with up to 40 percent velocity contrast were recovered and their locations and values were apparently determined accurately. Methods of estimating algorithm performance proved useful, though a fair amount of subjective input is necessary, such as minimization of large-wavenumber oscillations in the image through relaxation parameters and iteration. The assumption of straight rays seemed to cause few problems in the apparent reliability of the results, even in high-contrast media, though increased accuracy using a larger number of raypaths and

smaller pixels would require curved-ray algorithms. Differences in algorithms are minimal with performance depending upon the nature of the data set. Proper relaxation constraints must be applied and the proper number of iterations must be taken; otherwise, very poor reconstructions will result even though variances and discrepancies appear acceptable.

REFERENCES

Bois, P., La Porte, M., Lavergne, M., and Thomas, G., 1972, Well-to-well seismic measurements: Geophysics, 37, 471–480.

Clayton, R. W., and Comer, R. P., 1983, A tomographic analysis of mantle heterogeneities from body wave travel times (abstract): EOS Trans. Am. Geophys. Union, 62, 776.

Dines, K. A., and Lytle, R. J., 1979, Computerized geophysical tomography: Proc. Inst. Elect. and Electron. Eng., 67, 1065–1073.

Fawcett, J. A., and Clayton, R. W., 1984, Tomographic reconstruction of velocity anomalies: Bull. Seis. Soc. Am., 74.

Gordon, R., 1974, A tutorial on ART (Algebraic Reconstruction Techniques): Inst. Elect. and Electron. Eng. Trans. Nucl. Sci., NS-21, 78–93.

Gordon, R., Bender, R., and Herman, G. T., 1970, Algebraic reconstruction techniques (ART) for three-dimensional electron microscopy and X-ray photography: J. Theor. Biol., 29, 471–481.

Herman, G. T., Lent, A., and Rowland, S. W., 1973, ART: Mathematics and applications: J. Theor. Biol., 42, 1–32.

Herman, G. T., Lent, A., and Lutz, P. H., 1978, Relaxation methods for image reconstruction: Commun. Assoc. Comp. Mach., 21, 152–158.

King, M. S., and Paulsson, B. N. P., 1981, Acoustic velocities in heated block of granite subjected to uniaxial stress: Geophys. Res. Lett., 8, 699–702.

McMechan, G. A., 1983, Seismic tomography in boreholes: Geophys. J. Roy. Astr. Soc., 74, 601–612.

Menke, W., 1984, The resolving power of cross-borehole tomography: Geophys. Res. Lett., 11, 105–108.

Wong, J., Hurley, P., and West, G. F., 1983, Crosshole seismology and seismic imaging in crystalline rocks: Geophys. Res. Lett., 10, 686–689.